Detection of sub-superficial defects by infrared thermography in parts made by powder bed fusion with electron beam

Original
Detection of sub-superficial defects by infrared thermography in parts made by powder bed fusion with electron beam / Defanti, S., De Giorgi, S., Rizza, G., Colombini, G., Tognoli, E., Ayberk Gürbüz, A., Denti, L., Galati, M., Iuliano, L.. - ELETTRONICO. - 57:(2025), pp. 38-46. (17th Italian Manufacturing Association Conference, AITeM 2025 Bari (Italia) 10 September 2025 - 12 September 2025) [10.21741/9781644903735-5].

Publisher:
Materials Research Forum LLC

Published
DOI:10.21741/9781644903735-5

Detection of sub-superficial defects by infrared thermography in parts made by powder bed fusion with electron beam

Silvio DEFANTI[1,a *], Simone DE GIORGI[2,b], Giovanni RIZZA[2,c],
Giulia COLOMBINI[1,d], Emanuele TOGNOLI[1,e], Ahmet Ayberk Gürbüz[3,f],
Lucia DENTI[1,g], Manuela Galati[2,h] and Luca Iuliano[2,i]

[1]Department of Engineering ‘Enzo Ferrari’, University of Modena and Reggio Emilia, Via Vivarelli 10, 41125 Modena, Italy

[2]Department of Management and Production Engineering, Politecnico di Torino, Corso Duca degli Abruzzi 24, 10129 Torino, Italy

[3]Izmir Institute of Technology, Gülbahçe Kampüsü 35430 Urla İzmir, Turkey

[a]silvio.defanti@unimore.it, [b]simone.degiorgi@polito.it, [c]giovanni.rizza@polito.it,
[d]giulia.colombini@unimore.it, [e]emanuele.tognoli@unimore.it, [f]ayberkgurbuz96@gmail.com,
[g]lucia.denti@unimore.it, [h]manuela.galati@polito.it, [i]luca.iuliano@polito.it

Keywords: Powder Bed Fusion, Thermography, Inspection

Abstract. This study explores infrared thermography as a cost-effective alternative to computed tomography for detecting subsurface defects in parts produced by powder bed fusion with an electron beam (PBF-EB). Ti6Al4V specimens were produced with designed defects that mimic subsurface pores or discontinuities whose size and depth are typical of PBF-EB. Computed tomography (CT-scan) was used to collect information on the defect dimensions and coordinates accurately. The same samples were therefore analysed using Joule heating infrared thermography, applying electric current while an infrared camera recorded the temperature development on the surface of the sample. The joint analysis of CT scan and thermography data provided a comprehensive study on the limits of the inspection technologies, PBF-EB process, and measuring system in terms of defect size, depth, and the size-to-depth ratio. The results showed that the surface characteristics of the PBF-EB are critical for thermography.

Introduction

Additive manufacturing (AM), in particular powder bed fusion with electron beam (PBF-EB), has gained significant traction in various industries including aerospace, automotive and medical sectors, owing to its ability to efficiently produce complex metallic components for high-end applications. However, as AM becomes more widespread, the challenge of ensuring part qualification is also growing, particularly in applications where safety and reliability are critical.

Defects in AM parts originate from various sources and can significantly affect the morphology, size and geometry of the defect. These factors contribute to the varying degrees of detectability for such defects [1,2]. Common issues include porosity that may contain unmelted powder or trapped gases [3,4] and can range from small, spherical configurations to irregular shapes [5,6]. Gas-induced porosity includes trapped inert gas (spherical, 10-80 μm) and gas inclusions such as hydrogen pores (spherical, 5-20 μm) [7,8]. Process-induced porosity is caused by excess energy (keyhole porosity) or insufficient energy (lack of fusion). Keyhole porosity, where deep vapor cavities form in the melt pool, leads to spherical pores with a diameter of about 100 μm after collapse [9,10]. Lack of fusion consists of large and irregular cavity formations between neighbouring melt lines or layers (lengths of 400 μm to 600 μm and heights of 140 to 240 μm) [3,6,10,11,12]. Spatter particles can contribute to these voids by absorbing the energy destined for the powder bed. Balling defects, which occur when molten material separates into spherical shapes due to improper process settings, also contribute to the overall porosity(in the size range of 150 µm to 250 µm) [13]. Foreign debris inclusions and delamination due to insufficient interlayer adhesion further complicate defect profiles, together with cracks due to solidification stresses (150-200 µm long, 60-70 µm wide) [8,14].

To address these challenges, ex-situ IRT emerges as a promising inspection technique for detecting subsurface defects of AM components. This is particularly true for active methods that rely on an external excitation source to thermally stimulate the inspected part [15,16]. The effectiveness of IRT is closely linked to the excitation method used, as the different techniques have different advantages and limitations depending on the specific applications of non-destructive testing. In particular, current-excited thermography is characterised by a favourable signal-to-noise ratio and the ability to identify subsurface defects. However, it often requires a careful contact setup and is limited to electrically conductive materials.

Given the critical focus on qualification of PBF-EB produced metal parts, detailed assessment of defects and overall quality is paramount to meet stringent performance standards. IRT provides a fast, non-contact solution for defect detection and offers advantages such as ease of use and early identification of defective components [17,18,19]. Despite its demonstrated potential, the method faces significant challenges, including susceptibility to noise and limited ability to detect smaller or deeper defects. Recent studies have explored advanced post-processing algorithms and machine learning to improve the sensitivity of thermographic techniques, particularly in the detection of calibrated porosity defects. While larger defects can often be easily identified, reliable detection of smaller anomalies still requires advanced algorithms to reach limits of 127 µm in diameter and depth [20]. Spherical defects with a diameter to depth ratio greater than 3 were reliably detected, with improved probabilities using thermal signal reconstruction techniques. Convective stimulated thermography detected open defects up to 300 µm in size in an Inconel 718 sample, but was ineffective for smaller defects [21]. The ASTM report found that optical flash thermography and convective step heating detected open surface defects, with convective heating identifying defects down to 0.2 mm in size, although both methods had problems with deep-seated defects [1].

The current landscape of IRT applications related to AM remains limited, since there is a lack of standardised testing protocols and comprehensive benchmarking with established methods such as CT. This research aims to pave the way for a robust testing protocol dedicated to the detection of defects in PBF-EB components, utilising active thermography with Joule excitation. By conducting preliminary tests and using CT data as a reference, the work proposes a standardised methodology for defect detection and contributes to the overall qualification process for additive manufacturing.

Materials and methods

Samples with intentional defects were designed using Solidworks 2023 CAD software (Dassault Systemes) with a square constant cross-section of 10 mm x 10 mm and a gripping area to facilitate connection to the power supply. This preliminary study is part of a broader investigation that considers many types of defects that mimic those typical of PBF-EB. In this first step, the development of a method for non-destructive testing by thermography is proposed. For this purpose, samples with cylindrical defects open at one end and characterised by a diameter (hereafter size) between 0.5 and 1 mm and a depth below the continuous surface, under which they are located, between 0.25 and 2 mm are used. Fig. 1 shows four defects in the same sample with different diameters and at different depths under the same surface, called hereafter “target surface”, misaligned with each other to minimise current flow disruption. These defects are larger than those typically formed during PBF-EB, so they should be easier to detect with the chosen method, also as a result of at least partial emptying of the unconsolidated powder. More challenging defects will be considered at a later stage, when the test protocol will be more consolidated.

Joule excitation leads to localised heating of the defect, which is greater the larger the defect is. Thermographic observation of the target surface shows a thermal inhomogeneity that is all the more pronounced the higher the temperature reached by the defect and the shallower the defect. Consequently, the ratio of size-to-depth is a decisive factor for detectability. It is consistently stated in the literature that one of the limiting factors for the effectiveness of thermographic detection is the finish of the surfaces being analysed [20], and in PBF-EB the surface morphology is highly dependent on the relative orientation of the surface under consideration in the build chamber [2]. Therefore, different samples were built with defects below four target surface types: Upskin, Side, Downskin built on loose powder and Downskin built directly on the build platform and subsequently detached from it.

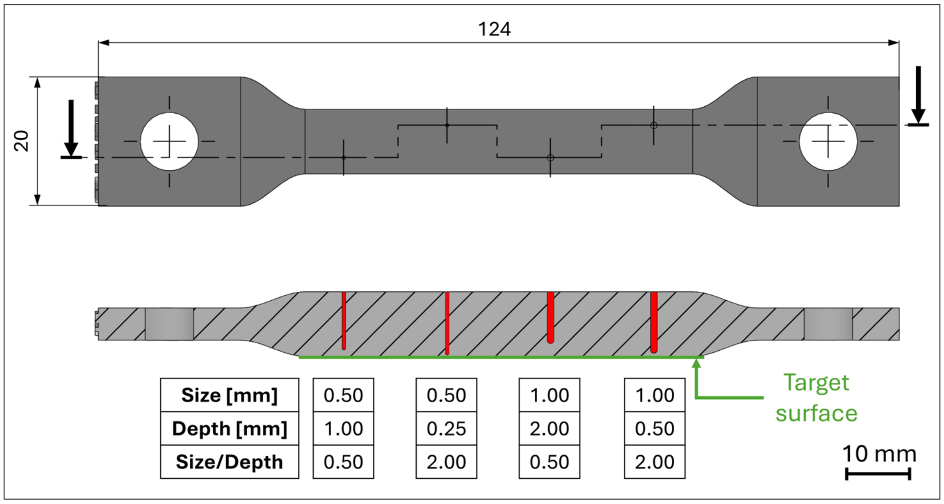

Size [mm]	0.50	0.50	1.00	1.00
Depth [mm]	1.00	0.25	2.00	0.50
Size/Depth	0.50	2.00	0.50	2.00

Fig. 1: Geometry of the samples showing the placement of the defects, their size, and depth below the target surface.

Samples were produced with an Arcam A2X PBF-EB system using standard Ti6Al4V powder with a size distribution ranging between 50 and 150 µm. Before the melting phase, each layer was preheated at 700 °C. The layer thickness was set equal to 0.050 mm. Details regarding the other process parameters are given in Table 1 [22]

Table 1: standard process parameters for Ti6Al4V

	Scan speed [mm/s]	Focus Offset [mA]	Beam current [mA]	Number of contours	Line offset [mm]
Contour (MultiBeam mode)	850	5	6	3	0.25
Hatching	1754	25	12	-	0.2

The surface topology of the samples was recorded using a Nikon LV 150 optical microscope (Nikon, Tokyo, Japan) equipped with a Confovis system. Specifically, an area of 4.5 x 2.5 mm^2 was scanned on the four types of surfaces. A 100x objective and a layer discretization of 0.50 µm were used.

The samples were CT scanned with a GE Phoenix V|tome|x S 240 with a voxel size of 20 µm to confirm the presence of the seeded defects and their detectability by tomography.

The thermography tests were performed with the following devices:

- Power supply: Xingtongli GKDM24-1000CVC, supplying DC current with a maximum voltage of 24 V and a maximum current of 1000 A.
- IR camera: Teledyne FLIR A700, placed at a distance of 40 mm from the target surface and equipped with a 2x macro lens that allows focussing on an area of 25.5 x 19.1 mm^2 with a sensor resolution of 640x480 pixels, resulting in a spatial resolution of 40 μm/pixel. The acquisition rate is 30 Hz.

Preliminary tests have shown that it is necessary to paint the target surface with a black, matt colour to avoid the effect of reflections. The sample to be analysed is placed on a fixed base in a partially enclosed chamber to limit interference from ambient light. The camera is positioned and focussed on the surface of the sample, then the recording begins and the current is applied for a few seconds. Before each test, it was checked that the temperature difference between the sample and the environment was less than 0.5°C. Each sample was tested 6 times, the repetitions of the experiments were randomized.

The recorded IR videos were post-processed with Matlab using the "FLIR Science File SDK for MatLab" to extract and process the individual IR frames as matrices. The first step in processing the data was to identify the captured image that had the highest defect contrast compared to the rest of the sample. For this purpose, the signal-to-noise ratio (SNR) was calculated as in [23,24]:

$$SNR = \frac{|\overline{T_d} - \overline{T_{nd}}|}{\sigma_{nd}} \tag{1}$$

Where:

$\overline{T_d}$ = average level of the signal in the defect region of interest (ROI), i.e. a rectangle closely enclosing the defect (Fig. 2)
$\overline{T_{nd}}$ = average level of the signal in the reference ROI, a hollow rectangular region (hatched in Fig. 2) obtained by offsetting the defect ROI.
σ_{nd} = standard deviation of the signal in the reference ROI

The defect is thus theoretically detectable if SNR > 1. In the initial development of the methodology, defect detection was based on the manual positioning of the reference ROI in an area adjacent to the defect. This approach was later replaced by the current automated solution, based on the self-referencing method proposed by Usamentiaga et al. [24], which ensures a more reliable adaptation to the defect shape while eliminating the risk of arbitrarily selecting a non-representative region.

Various approaches were tested to automatically determine the size of the defect from the thermographic images. These included: i) fitting a Gaussian curve to the temperature profile crossing the defect and evaluating the start and end of the peak or full width at half maximum; ii) mathematically analysing the temperature profile across the defect or its derivative.

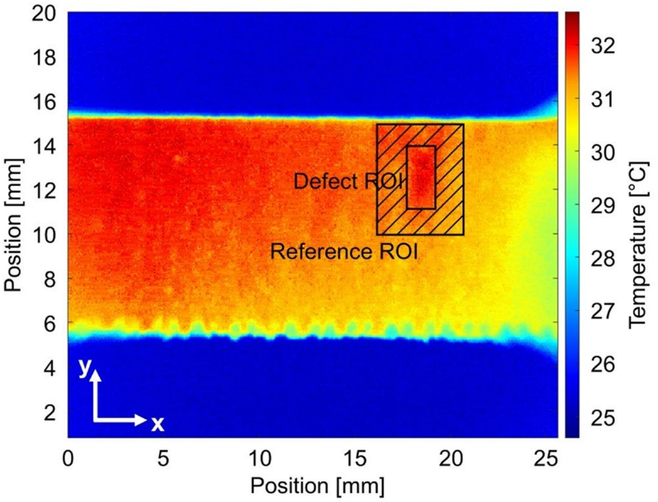

Fig. 2: Representation of the ROIs for SNR calculation.

Results and Discussion

The results of the confocal measurements on the target surfaces are shown in Fig. 3 together with the 3D average areal surface roughness S_a. The upskin has the most even surface while the roughness of the downskin varies depending on the costruction on the build platform or the loose powder. The side surfaces have the highest roughness of 38.4 µm. These variations significantly impact defect detectability, assessed using the SNR methodology. This effect is clearly illustrated in Fig. 4, where the same defect is analyzed on both the downskin and upskin surfaces. The results differ considerably, with an SNR of 2.36 in one case, while in the other it is close to the minimum detection threshold of 1, demonstrating a clear decline in detection efficiency as surface roughness increases.

Detection is also strongly influenced by the size and depth of the defects. Table 2 shows the nominal values and the corresponding SNR calculations for the individual artefacts produced. Smaller defects and greater depths reduce detectability, which often leads to non-detection and thus illustrates the limitations of this inspection technology. Defects at a depth of 2 mm mostly remain undetected, even at larger sizes, while a 0.5 mm defect is only detected at a shallow depth of 0.25 mm. All defects were successfully detected with tomography instead.

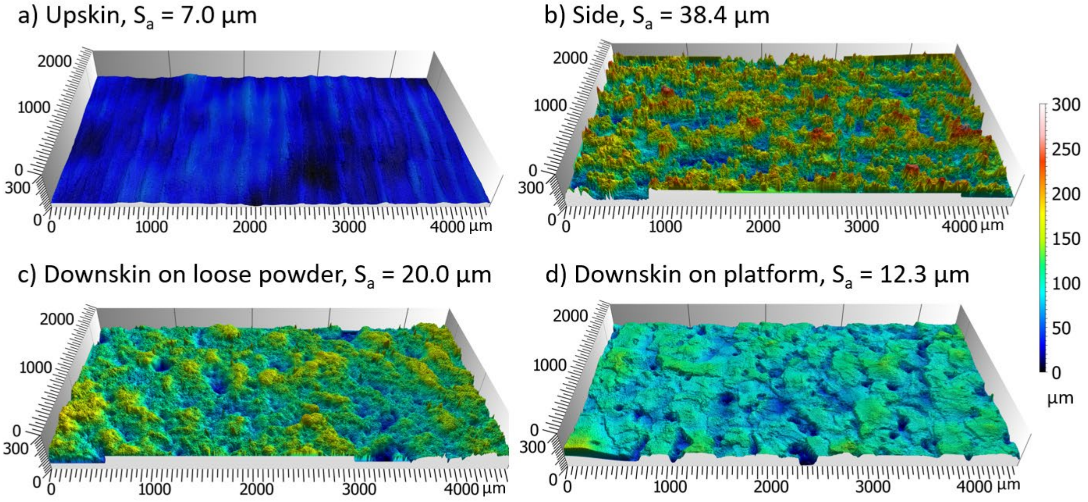

Fig. 3: Confocal maps of the target surfaces.

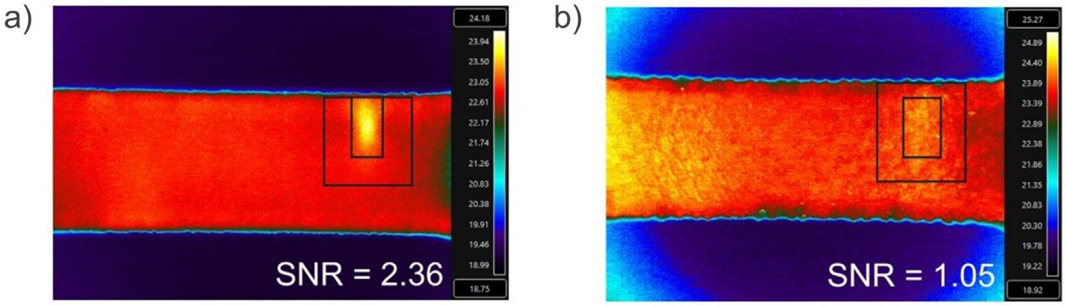

Fig. 4: Results of the SNR calculation for the defect with 1 mm diameter and 0.5 mm depth in the case of downskin (a) and upskin (b) target surface.

The thermographic images were also processed to determine the defect size. Robust results were obtained using the following method:

- An additional Measurement ROI was determined, i.e. a rectangle with a large base crossing the defect in the direction of current flow (x) and a height smaller than the hot area in the y-direction (Fig. 5a).
- A temperature profile was calculated by averaging the temperature values along the y-direction for each x-position (Fig. 5b).
- The experimental data were fitted with a three-term Gaussian function and the first derivative of the Gaussian profile was calculated (Fig. 5c).
- The defect size was determined as the x-distance between the maximum and minimum positions (Fig. 5d).

Table 2: Results of the thermographic analysis.

Target surface	**Nominal**		**Thermography**				**Target surface**	**Nominal**		**Thermography**			
	Size [mm]	**Depth [mm]**	**SNR**		**Size [mm]**			**Size [mm]**	**Depth [mm]**	**SNR**		**Size [mm]**	
			Avg.	**S.D.**	**Avg.**	**S.D.**				**Avg.**	**S.D.**	**Avg.**	**S.D.**
Up	0.5	1.00	0.43	0.05	-	-	Down	0.5	1	0.63	0.10	1.26	0.27
	0.5	0.25	1.90	0.38	0.86	0.07		0.5	0.25	1.03	0.10	1.26	0.16
	1	2	0.20	0.09	-	-		1	2	0.39	0.05	-	-
	1	0.5	2.36	0.20	1.02	0.05		1	0.5	1.05	0.05	1.46	0.39
Side	0.5	1	0.27	0.06	-	-	Down-platform	0.5	1	1.26	0.25	0.77	0.10
	0.5	0.25	0.59	0.15	-	-		0.5	0.25	1.52	0.27	0.88	0.10
	1	2	0.38	0.07	-	-		1	2	1.13	0.14	1.66	0.06
	1	0.5	1.74	0.08	1.28	0.05		1	0.5	2.89	0.42	0.99	0.09

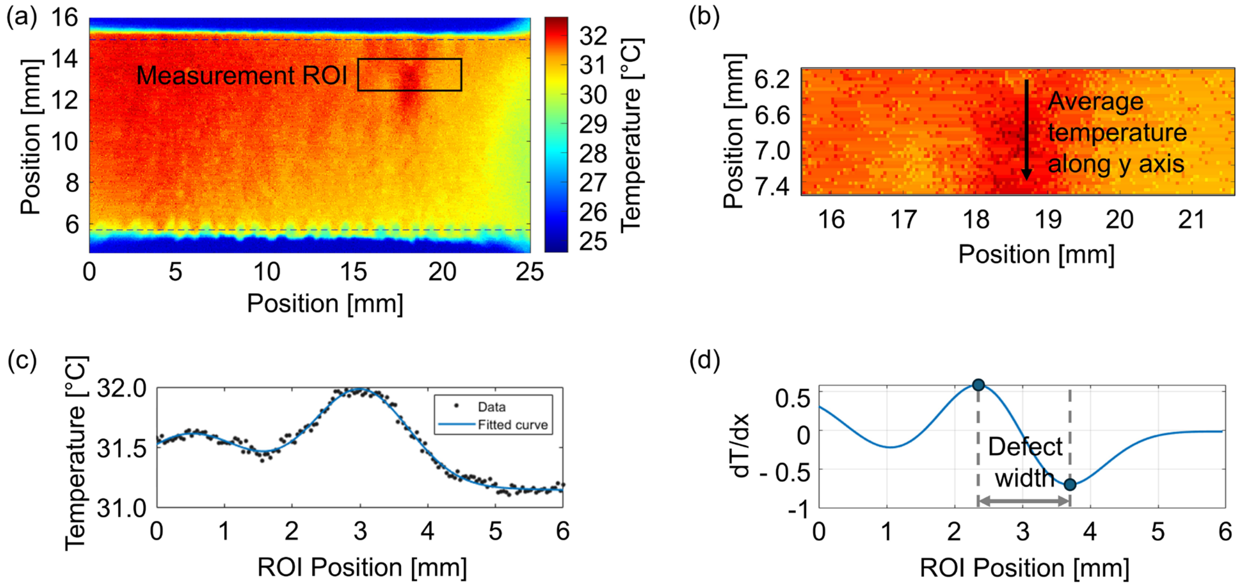

Fig. 5: Defect measurement procedure: a) identification of the measurement ROI, b) magnification of the measurement ROI, c) temperature vs. position plot with the fitted Gaussian curve, d) indication of the defect width in the first derivative curve.

Conclusions

This study aims to define a robust methodology for the application of active IRT with Joule excitation for defect detection in PBF-EB components. Open cylindrical defects of different sizes (0.5–1 mm) and depths (0.25–2 mm) were intentionally introduced into the fabricated samples, which were used as test artefacts for the development of an NDT procedure. Key achievements include an automated and reliable method for SNR calculation and Gaussian-based automatic defect sizing, as well as the identification of a robust test setup. In particular, the experimental measurements have shown that detectability is critically affected by the morphology of the target surface, leading to a reduction in detection efficiency for rougher surfaces, and by the dimensional characteristics of the defects analysed, with defects at a depth of 2 mm not being detected even at larger sizes, and a 0.5 mm diameter defect being detected at a shallow depth of only 0.25 mm. IRT is thus confirmed as a valuable technique for rapid non-destructive evaluation, and this study represents the first step in the evaluation of this method compared to accurate and time-consuming alternatives such as tomography.

References

[1] ASTM International and ISO/ASTMTR52905, *Additive Manufacturing of Metals—Nondestructive Testing and Evaluation—Defect Detection in Parts*. ASTM International100 Barr Harbor Drive, PO Box C700, West Conshohocken, PA 19428-2959, 2023. https://doi.org/10.1520/ISO/ASTMTR52905-EB

[2] M. Galati, “Electron beam melting process,” in *Additive Manufacturing*, Elsevier, 2021, pp. 277–301. https://doi.org/10.1016/B978-0-12-818411-0.00014-8

[3] ASTM International and E3166-20, “Standard Guide for Nondestructive Examination of Metal Additively Manufactured Aerospace Parts After Build,” Feb. 01, 2020, *ASTM International, West Conshohocken, PA*. https://doi.org/10.1520/E3166-20

[4] Y. Zhu, Z. Wu, W. D. Hartley, J. M. Sietins, C. B. Williams, and H. Z. Yu, “Unraveling pore evolution in post-processing of binder jetting materials: X-ray computed tomography,

computer vision, and machine learning," *Addit Manuf*, vol. 34, p. 101183, Aug. 2020. https://doi.org/10.1016/j.addma.2020.101183

[5] Y. Gui, K. Aoyagi, and A. Chiba, "Development of macro-defect-free PBF-EB-processed Ti–6Al–4V alloys with superior plasticity using PREP-synthesized powder and machine learning-assisted process optimization," *Materials Science and Engineering: A*, vol. 864, p. 144595, Feb. 2023. https://doi.org/10.1016/j.msea.2023.144595

[6] Z. Snow, A. R. Nassar, and E. W. Reutzel, "Invited Review Article: Review of the formation and impact of flaws in powder bed fusion additive manufacturing," *Addit Manuf*, vol. 36, p. 101457, Dec. 2020. https://doi.org/10.1016/j.addma.2020.101457

[7] T. Liu, S. Guessasma, J. Zhu, W. Zhang, H. Nouri, and S. Belhabib, "Microstructural defects induced by stereolithography and related compressive behaviour of polymers," *J Mater Process Technol*, vol. 251, pp. 37–46, Jan. 2018. https://doi.org/10.1016/j.jmatprotec.2017.08.014

[8] P. Charalampous, I. Kostavelis, and D. Tzovaras, "Non-destructive quality control methods in additive manufacturing: a survey," *Rapid Prototyp J*, vol. 26, no. 4, pp. 777–790, Mar. 2020. https://doi.org/10.1108/RPJ-08-2019-0224

[9] X. Yang, Y. Li, and B. Li, "Formation mechanisms of lack of fusion and keyhole-induced pore defects in laser powder bed fusion process: A numerical study," *International Journal of Thermal Sciences*, vol. 188, p. 108221, Jun. 2023. https://doi.org/10.1016/j.ijthermalsci.2023.108221

[10] C. Du *et al.*, "Pore defects in Laser Powder Bed Fusion: Formation mechanism, control method, and perspectives," *J Alloys Compd*, vol. 944, p. 169215, May 2023. https://doi.org/10.1016/j.jallcom.2023.169215

[11] M. S. Palm, B. Diepold, S. Neumeier, H. W. Hoeppel, M. Goeken, and M. F. Zaeh, "Detection and effects of lack of fusion defects in Hastelloy X manufactured by laser powder bed fusion," *Mater Des*, vol. 230, p. 111941, Jun. 2023. https://doi.org/10.1016/j.matdes.2023.111941

[12] R. Zhao, A. Shmatok, R. Fischer, and B. C. Prorok, "Investigation of Causal Relationships between Printing Parameters, Pore Properties and Porosity in Laser Powder Bed Fusion," *Metals (Basel)*, vol. 13, no. 2, p. 330, Feb. 2023. https://doi.org/10.3390/met13020330

[13] W. Wang *et al.*, "Processing defect, microstructure evolution and mechanical properties of laser powder bed fusion Al-12Si alloys," *Journal of Materials Research and Technology*, vol. 26, pp. 681–696, Sep. 2023. https://doi.org/10.1016/j.jmrt.2023.07.231

[14] N. Kouraytem *et al.*, "Solidification crack propagation and morphology dependence on processing parameters in AA6061 from ultra-high-speed x-ray visualization," *Addit Manuf*, vol. 42, p. 101959, Jun. 2021. https://doi.org/10.1016/j.addma.2021.101959

[15] R. Yang and Y. He, "Optically and non-optically excited thermography for composites: A review," *Infrared Phys Technol*, vol. 75, pp. 26–50, Mar. 2016. https://doi.org/10.1016/j.infrared.2015.12.026

[16] B. Wiecek, "Review on thermal image processing for passive and active thermography," in *2005 IEEE Engineering in Medicine and Biology 27th Annual Conference*, IEEE, 2005, pp. 686–689. doi: 10.1109/IEMBS.2005.1616506

[17] C. Meola, S. Boccardi, and G. M. Carlomagno, *Infrared Thermography in the Evaluation of Aerospace Composite Materials*. Elsevier, 2015

[18] A. Heifetz, X. Zhang, J. Saniie, and W. Cleary, “Detection of Defects in Additively Manufactured Metallic Materials with Machine Learning of Pulsed Thermography Images,” Argonne, IL (United States), Sep. 2020. doi: 10.2172/1673390

[19] N. Montinaro, D. Cerniglia, and G. Pitarresi, “Defect detection in additively manufactured titanium prosthesis by flying laser scanning thermography,” *Procedia Structural Integrity*, vol. 12, pp. 165–172, 2018. https://doi.org/10.1016/j.prostr.2018.11.098

[20] E. D’Accardi, S. Altenburg, C. Maierhofer, D. Palumbo, and U. Galietti, “Detection of Typical Metal Additive Manufacturing Defects by the Application of Thermographic Techniques,” in *The 15th International Workshop on Advanced Infrared Technology and Applications*, Basel Switzerland: MDPI, Sep. 2019, p. 24. doi: 10.3390/proceedings2019027024

[21] C. G. Kolb *et al.*, “An investigation on the suitability of modern nondestructive testing methods for the inspection of specimens manufactured by laser powder bed fusion,” *SN Appl Sci*, vol. 3, no. 7, p. 713, Jul. 2021. https://doi.org/10.1007/s42452-021-04685-3

[22] M. Galati and S. Defanti, “Additive Manufacturing of Locally Weakened Parts to Obtain a Designed Fracture,” *Metals and Materials International*, vol. 30, no. 2, 2024. https://doi.org/10.1007/s12540-023-01506-7

[23] F. J. Madruga, C. Ibarra-Castanedo, O. M. Conde, J. M. López-Higuera, and X. Maldague, “Infrared thermography processing based on higher-order statistics,” *NDT & E International*, vol. 43, no. 8, pp. 661–666, Nov. 2010. https://doi.org/10.1016/j.ndteint.2010.07.002

[24] R. Usamentiaga, C. Ibarra-Castanedo, and X. Maldague, “More than Fifty Shades of Grey: Quantitative Characterization of Defects and Interpretation Using SNR and CNR,” *J Nondestr Eval*, vol. 37, no. 2, p. 25, Jun. 2018. https://doi.org/10.1007/s10921-018-0479-z